Persistent Hot-Spot Mix in Cryogenic Direct-Drive Fusion Experiments

R. C. Shah,[*] D. Cao, I. V. Igumenshchev, V. N. Goncharov, K. S. Anderson, K. A. Bauer, R. Betti, M. J. Bonino, E. M. Campbell, A. Colaïtis, T. J. B. Collins, K. Churnetski, C. J. Forrest, D. H. Froula, V. Yu. Glebov, V. Gopalaswamy, D. R. Harding, S. X. Hu, R. T. Janezic, J. Kwiatkowski, A. Lees, S. F. B. Morse, S. Miller, D. Patel, S. P. Regan, S. Sampat, C. A. Thomas, and D. Turnbull

Laboratory for Laser Energetics, University of Rochester, Rochester, New York 14623-1299, USA

We show that an x-ray emission signature associated with acceleration phase mass injection [R. C. Shah *et al.*, Phys. Rev. E **103**, 023201 (2021)] correlates with poor experimental hot-spot convergence and a reduced neutron production relative to expectations. It is shown that with increased target mass as well as with higher-design adiabats, this signature is reduced, whereas with increased debris on the target, the signature is increased. We estimate that the vapor region in typical best designs may have up to 2× the assumed hydrogen mass at the start of deceleration.

From the very earliest days of inertial confinement fusion, one of the most significant risks to ignition has been amplification of small perturbations on the ablation front due to Rayleigh-Taylor instability [1]. As a result, there can be "mix" of ablator or peripheral cold fuel into the central hot spot. Even in the absence of radiative losses, the mass injection and associated nonradial flows will reduce compression and compromise the hot-spot pressure and fuel areal density [2]—critical parameters for ignition and gain. Here we report on strong signatures of hot-spot mix in direct laser-driven cryogenic implosion experiments conducted at the subignition-scale 30-kJ OMEGA Laser.

Whereas previous studies of hot-spot mix were sensitive only to high Z in the hot spot [3–7], the technique used here can indicate mixing of additional hydrogen into the hot spot from the peripheral dense fuel. This is of particular importance for direct drive in which only a thin plastic overcoat precedes a dominant ablation phase in hydrogen. Even with such a limited reservoir of plastic, experiments with specialized shells that included germanium dopant in a small outermost layer of the plastic have shown the germanium to reach the hot spot [7]. This strongly suggests much greater amounts of hydrogen-on-hydrogen mix.

In our Letter, we characterize a discrepancy between observed and modeled in-flight images taken at the time of onset of x-ray self-emission from the hot spot in cryogenic experiments [8]. Previously, it was shown that for an implosion design with low shell adiabat $\alpha = P_A/P_F$ (the ratio of shell pressure to its Fermi degenerate pressure) of $\alpha \sim 2$, radiation hydrodynamic modeling that included coherent effects of laser speckle (i.e., laser imprinting) led to a fully broken dense fuel layer during acceleration.

Both deuterium and tritium (DT) and plastic were transported to the developing hot spot, and in the calculated images of soft x-ray self-emission, the central region brightened earlier (and at larger radius) than in the no-imprint calculations. Gated images in the experiment were in good agreement for this low adiabat case. However, when α was increased, and thus expected to mitigate imprint growth, an emission discrepancy persisted. As discussed in Ref. [8], two broad hypotheses emerged to describe this residual discrepancy and performance deficits: (i) additional, unmodeled hot-spot mix and (ii) "1D" physics, i.e., fundamental issues in the 1D reference calculation itself such as errors of shock timing, poor shock release, unwanted shock formation, or even kinetic plasma effects [8–10]. Mitigation and scaling of the OMEGA experiments to fusion with energy gain is dependent on distinguishing between these different frameworks of understanding the current implosion experiments.

Here we show new data that provide strong support that it is mix which causes this anomalous x-ray signal and is a principal source of performance degradation in current direct-drive implosions. The new data show that the anomalous emission signature is reduced for higher mass implosions, increased for a target with elevated levels of ablator particulate, correlates with stagnation metrics, and show an indication from hot-spot images of a peripheral modification. A simulation which includes surrogate ablator features shows that the associated acceleration phase mass injection causes both the acceleration phase emission advance and stagnation phase hot-spot image modification. Based on the empirical trends and surrogate calculations, a typical high-performance implosion may have up to a 2× increase of hot-spot mass at the start of deceleration compared to a 1D calculation. Such mix may provide an explanation as to why high-performance implosions are

---
[*]Contact author: rahulshah@lle.rochester.edu

unresponsive to beam smoothing [11] and thus why optima are not able to be explained with the nominal radiation hydrodynamic models [12].

The cryogenic implosions discussed are conducted with the same standards of operation of the 60-beam OMEGA Laser as used to pursue ignition-relevant metrics, including maximal smoothing of coherent speckles in the laser beams. The experiments had a nominal laser power of 20 TW and an energy of 25 kJ with pulse shapes changed to explore differing adiabats and target variations. The targets were 8-μm-thick, 860-μm-diameter spherical plastic shells surrounding a cryogenic ice layer of DT. The thickness of the cryogenic layer was varied within the range of 50 to 80 μm. For a companion thicker target, key factors that dramatically reduce penetration of perturbations are a reduction of the in-flight aspect ratio (IFAR), increased role of ablative stabilization, and reduced seeding of imprint [13]. Prior to the shots, the targets were also imaged in a characterization station where they were commonly observed to show evidence of particulate condensates that originated from beta-decay-induced damage of targets and other materials present during the filling [14]. Typically, external condensates are sublimated away; however, in our experiments one target showed > 20 external features that persisted and were observed in limb images with heights estimated from a few to 20 μm. As will be shown, this target was found to exaggerate the observed signatures over nominal cases.

To diagnose the onset of the hot-spot self-emission, we use pinhole imaging with an x-ray framing camera. Each camera records up to 16 images with ∼20-μm point-spread function and 40-ps time integration with response such that the average x-ray energy is 0.8 keV. The image acquisition is timed so as to capture flight after the carbon-deuterium shell has been fully ablated and ablation occurs in the dense DT plasma. Such images initially show only a peaked annulus that provides a fiducial of the ablation front and acts as a reference signal level for the rapidly increasing central emission of the hot spot (the analysis is very similar to that of Ref. [8]). The individual frames, typically obtained from two independent cameras, are used to plot the core emission versus ablation-front radius and establish upper and lower bounds on a radius at which a threshold core emission is reached. The soft x-ray emission from the hot spot depends on target design and pulse shape. To account for these characteristics in the absence of 3D instability, we rely on a detailed comparison to images calculated from the 1D radiation hydrodynamic code LILAC [15] using the Spect3D postprocessing software (Prism Computational Sciences, Inc., Madison, WI). We then report the normalized difference in the onset radius between the experiment and 1D model as $\Delta R = (R_{\mathrm{expt}} - R_{\mathrm{1D}})/R_{\mathrm{1D}}$. In the top left inset of Fig. 1(a), we include an example of a framed image at the onset of the central emission. Adjacent is a comparison of the data (angle-averaged profile, solid
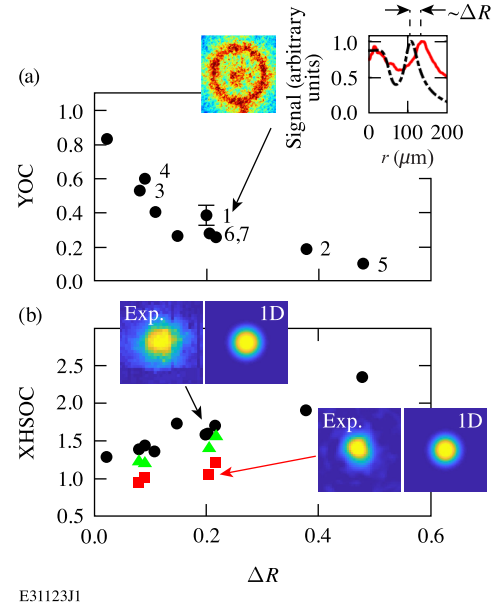

FIG. 1. Correlations of stagnation observables with ΔR. (a) Correlation with 1D normalized neutron yield (YOC). Selected implosions discussed in the Letter are numbered. Inset shows gated image (box size of 400 μm) at the time of the onset of central emission (red solid line) and comparison with 1D calculation (black dashed line). (b) Correlation with 1D normalized x-ray hot-spot size (XHSOC) obtained for all shots at a mean detected x-ray energy of ∼5 keV (black circles). In some cases, measurements were also made with an additional imager at similar x-ray energy (green triangles) and another at ∼2× higher photon energy (red squares). Insets show images for implosion no. 6 (box size of 80 μm).

red line) and image from the 1D calculation (dashed black line) showing that in the calculation, a comparable ratio of central emission to limb emission requires greater convergence of the ablation front.

The primary plot of Fig. 1(a) shows that the measured DT yield relative to its 1D value [yield over clean (YOC)] correlates to ΔR, thus suggesting the emission signature is caused by a mechanism that also strongly degrades the neutron yield. The YOC values are corrected for $\ell = 1$ asymmetry using the ion temperature variation and also compensated for target aging by normalizing to a 1D calculation, which accounts for ^{3}He accumulation in the vapor due to T breakdown [16]. The effect of ^{3}He buildup in determining the 1D expected emission turn-on is rather small but included and typically causes ∼0.05 reduction of ΔR.

Parameters for all the implosions are provided in Table I. We first discuss companion shots for which the payload (DT layer thickness) was increased. Implosion no. 5, for which we have the largest emission discrepancy and lowest YOC, was an $\alpha \sim 2$ design with a 50-μm DT layer. As summarized above and previously reported [8], the observed emission discrepancy and YOC were predicted by 3D modeling with imprint. Implosion nos. 6 and 7 were

TABLE I. Stability-related parameters for the studied cryogenic implosions: α is mass-averaged adiabat at two-thirds convergence, th_{DT} is the initial nominal DT layer thickness, IFAR is the in-flight aspect ratio at this time, and V_i is peak implosion velocity. The implosions (1–4) and (5–7) provide comparisons in IFAR at similar adiabats by changing the thickness of the cryogenic layer. Peak powers were within 6%, total energy 4%, and target outer diameter 1%. Note for shots overlapping with those of Ref. [8] the use of a single standardized mass-averaged definition has changed some values though not in a way as to influence conclusions.

| Shot	α	th_{DT} (μm)	IFAR	V_i (cm/ns)
(1) 94 008	3.4	50	24.2	388
(2) 94 006[a]	3.5	50	24.8	386
(3) 105 176	3.8	80	14.3	271
(4) 105 179	4.1	80	14	271
(5) 94 013	1.6	50	37.3	388
(6) 105 182	2.1	80	16	250
(7) 105 184	2.2	80	15.3	250
(8) 105 451	6.3	80	10	263
(9) 79 626	9.7	65	19.7	333
(10) 105 448	2.6	80	16.5	257

[a]Target characterization showed 2×10^4 μm^2 defect surface area associated with condensate particulates, $\sim 3\times$ typical coverage.

designed to have a similar adiabat but with an 80-μm DT layer such that hydrodynamic damage would be mitigated. The reduction of emission discrepancy and increased YOC are consistent with this expectation, although, as will be discussed later, we are unable to reconcile the persistence of a residual level of discrepancy with laser imprint. Implosion no. 1 indicates the $\alpha \sim 3.5$ design with 50-μm DT layer, which, as has been summarized, shows an emission discrepancy that is not predicted to result from laser imprint. (The calculated yield with the 3D imprint model relative to the 1D yield for this implosion is $\sim$80%). Implosion nos. 3 and 4 are thicker, slower companions of implosion no. 1 designed to be at a similar adiabat for which we again see reduction of emission discrepancy and improvement of YOC. Implosion no. 2 was in all aspects a repeat of implosion no. 1 with the exception that the target in this case showed exceptional outer limb debris. Its emission discrepancy increase and YOC decrease correlate well with the others, providing additional support that a hydrodynamic instability-driven mix is underlying these observations.

Figure 1(b) shows the 1D normalized dependence of the outer contour size of the time-integrated x-ray self-emission of the hot spot with the black solid circles obtained from a Kirkpatrick-Baez microscope [17]. The response determined by reflectivity, filtration, and camera is centered at $\sim$5.5 keV. This provides a completely independent measurement, reinforcing the correlation between increasing emission discrepancy and degradation

of implosion quality from the 1D design. For a few available cases, the normalized hot-spot size as determined from pinhole images with spectral response at approximately the same average energy but integrating over a larger spectral range are shown with the solid green triangles. In contrast to the low-energy images, the solid red squares show the same comparison but obtained at $\sim$10 keV by the use of large apertures and penumbral analysis [6]. At higher x-ray energies, the image samples increasingly hotter and interior regions of the hot spot. The high-energy imager records an emissivity weighting comparable to that of the DT reaction rate $\rho^2 \langle \sigma_v \rangle \sim \rho^2 (kT)^4$, where ρ is mass density, $\langle \sigma_v \rangle$ is the DT reactivity, and T the temperature. The low-energy imager dramatically enhances the periphery as it sees an emissivity $\sim \rho^2 T^2$ or a P^2 dependence, where P is the hot-spot pressure (see Refs. [5,18]). From the data, it is apparent that as the emission discrepancy increases, and the hot-spot contour increases relative to 1D, that the size increase occurs disproportionately in the low-temperature periphery of the implosion. Mix into the hot spot can cause a breakdown of the typical isobaric conditions and thereby expand the hot-spot periphery, as shown later in this Letter.

The 3D simulations of imprint are limited and available for only two of the shots; therefore, we have implemented a well-established growth factor and saturation model that extends the quantification of shell breakup by imprint over all the cases. The model is used to determine an estimated bubble amplitude h_b when the shell is at one third its initial size (roughly the radius of emission onset). To determine the bubble height, we begin with the spherical harmonic mode spectra of areal density modulation at shock breakout taken from calculations with the high-resolution 3D ASTER code for similar types of implosions [13,19,20]. (We note ASTER spectra are similar to those from the 2D code DRACO [13,21] for which validation experiments have indicated reasonable agreement [22–24].) This input is then amplified by linear growth factors [25] until the growth, if necessary, is modified by the broadband Haan saturation model [26]; h_b is a rms sum over all modes. This calculation accounts for the reduction of the growth factor $\gamma = \int [\sqrt{Akg(t)} - BkV_a(t)] dt$ due to ablation velocity V_a, where A and B are fit parameters for a given material, k is the wave number, and g the acceleration. Figure 2(a) shows, with solid black circles, the emission discrepancy plotted against the shell thickness unperturbed by imprint determined by this procedure $\Delta - h_b$, where Δ is the 1D shell thickness at this convergence. A negative value of $\Delta - h_b$ indicates imprint bubbles have completely traversed the cold fuel and occurs only for implosion no. 5 (thin layer and low adiabat). The emission discrepancy determined from 3D ASTER is shown with the green $\times$'s for the two available cases. For the case of implosion no. 5, for which the DT shell is fully penetrated, the 3D calculation correctly predicts a large emission discrepancy. For implosion no.
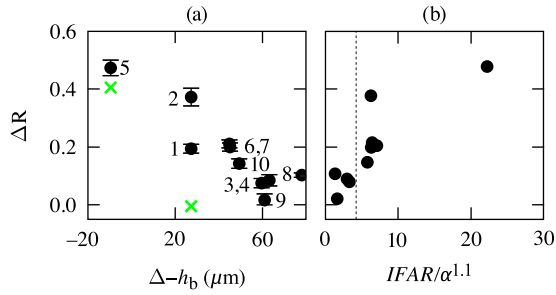
E31124J1

FIG. 2. (a) Emission discrepancy ΔR is plotted against in-flight shell thickness that is unperturbed by imprint $\Delta - h_b$, where Δ is the shell width at one third the initial size (roughly the radius of emission onset), and h_b is the estimated bubble amplitude due to laser imprint at this time. The green ×'s indicate the predicted ΔR from 3D simulation with laser imprint. (b) ΔR is plotted against a generalized stability parameter. Implosion no. 2 was known to have additional debris on the ablator. The vertical dotted line indicates the stability parameter for a typical high-performance cryogenic implosion.

1 with a higher adiabat, the calculation with imprint does not predict an emission discrepancy, consistent with the positive abscissa value from the growth factor model. The full 3D ASTER calculation of implosion no. 1 was repeated with approximately double the perturbation mode spectrum from imprint. In that supplementary calculation, the dense fuel was further penetrated, but remained intact, and thus there was still no significant predicted emission discrepancy. Moving rightward in Fig. 2(a), h_b falls exponentially as Δ increases, and thus imprint is ruled out as a source of shell penetration. Nonetheless, from Fig. 2(a) it is evident that a correlation is present, which is indicative of a dependence on parameters governing the sensitivity to hydrodynamic instability.

This dependence is better shown [see Fig. 2(b)] using a generalized stability metric of $\text{IFAR}/\alpha^{1.1}$, originally put forward by Goncharov et al. [27] and previously correlated with the emission discrepancy in Ref. [8]. The inclusion here of primarily IFAR changes (increased mass at similar adiabat companion shots) strongly supports the mix hypothesis as the dominant cause of the emission advance. Implosion no. 2, for which there was a change in initial conditions, is a noticeable and expected outlier. The smaller outlier at the leftmost side of the plot may indicate uncontrolled variations or an enhanced feature-driven instability growth (discussed below) due to a particularly strong first shock created by a picket intensity 2× that of any other implosion in the set. The stability position of a typical high-performance cryogenic implosion is also indicated by the dotted vertical line. Experiments have recently shown an insensitivity of such a design to variations of the imprint around nominal levels, despite significant underperformance [11]. This Letter suggests its performance is impacted by hot-spot mix from a source other than imprint.

A candidate for the source of mix is the role of target features. Electron microscopy, as well as confocal microscopy, have been used to show that micron-scale cracks, voids, nodules, and surface features are typical in the plastic used in these experiments [28]. The ablator is known to undergo material stresses and bond changes due to tritium-induced radiation damage during the diffusion fill process [29]. Furthermore, cryogenic targets may accumulate additional debris from the time of evaluation at a characterization station to insertion and mechanical shroud pull. Previously, full-sphere 2D numerical studies of target features have shown that such features can lead to in-flight jetting into the central low-vapor region during acceleration [2]. To test if signatures as described here could result, an exploratory simulation was conducted with 3D ASTER in which 50 divots of 10-μm diameter and 2-μm maximum depth in the ablator were used as computationally tractable surrogates for features that might induce mass jetting [12]. Referring to Fig. 3(a), calculated in-flight images near the end of the acceleration phase show an emission advance readily arises due to the mass injection. Electron temperature and density profiles obtained near peak neutron production were also used to calculate angle-averaged, chord-integrated images. These results are summarized in the middle and upper panels of Fig. 3(b) and show distinct changes in what is observed at high and low photon energies, consistent with the trend observed in the data [Fig. 1(b)]. Although the ion temperature is significantly reduced when defects are included, due to an increased equilibration, the electron temperature T_e remains peaked at nearly the same value. As shown in the bottom of Fig. 3(b), the shoulder of the T_e profile
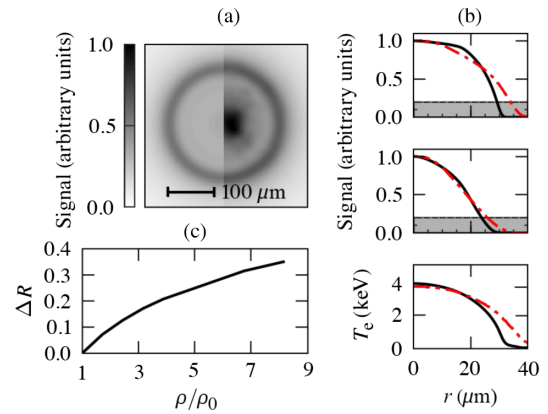
E31125J1

FIG. 3. (a) Calculated in-flight soft x-ray image from 3D ASTER for uniform calculation (left-hand side) and the case of 50 ablator divots (right-hand side). (b) Chord-integrated x-ray self emission at 4 keV (top panel) and 12 keV (middle panel), and angle-averaged electron temperature (T_e) profile (bottom panel), all at the time of peak neutron production. The uniform case is shown with a solid black line and defect result with a dashed red line. (c) Variation of ΔR from 1D simulations as a function of the increasing initial vapor mass in void (ρ/ρ_0).

extends to larger radii for the defects case and leads to the disproportionate change of the high- and low-energy imagers. To estimate the mass injection associated with the emission discrepancy measured in the experiments, we have conducted a series of 1D calculations with increasing initial vapor mass density [Fig. 3(c)]. For $\Delta R \sim 0.1$ as is implied by Fig. 2(b) for the high-performance implosion, this exercise indicates $\sim 2\times$ the nominal hot-spot mass (corresponding to $\sim 0.5\%$ injection of the DT payload mass).

In conclusion, laser imprinting is a significant source of perturbation and hot-spot mix in direct drive, but as implosions are given sufficient stability, imprint is mitigated. Here we have shown results which indicate that hot-spot mix persists in this regime and that jetting by isolated features provides a plausible explanation for acceleration and stagnation phase observations. Motivated by these findings, target characterizations, numerical simulations, and focused experiments are being used to more conclusively identify the cause of the mix, which will then enable quantitative prediction of the impact on performance at ignition scales.

[1] J. Nuckolls, L. Wood, A. Thiessen, and G. Zimmerman, Laser compression of matter to super-high densities: Thermonuclear (CTR) applications, Nature (London) **239**, 139 (1972).

[2] I. V. Igumenshchev, V. N. Goncharov, W. T. Shmayda, D. R. Harding, T. C. Sangster, and D. D. Meyerhofer, Effects of local defect growth in direct-drive cryogenic implosions on omega, Phys. Plasmas **20**, 082703 (2013).

[3] S. P. Regan *et al.*, Hot-spot mix in ignition-scale inertial confinement fusion targets, Phys. Rev. Lett. **111**, 045001 (2013).

[4] T. Ma *et al.*, Onset of hydrodynamic mix in high-velocity, highly compressed inertial confinement fusion implosions, Phys. Rev. Lett. **111**, 085004 (2013).

[5] R. Epstein, V. N. Goncharov, F. J. Marshall, R. Betti, R. Nora, A. R. Christopherson, I. E. Golovkin, and J. J. MacFarlane, X-ray continuum as a measure of pressure and fuel–shell mix in compressed isobaric hydrogen implosion cores, Phys. Plasmas **22**, 022707 (2015).

[6] R. C. Shah *et al.*, Bound on hot-spot mix in high-velocity, high-adiabat direct-drive cryogenic implosions based on comparison of absolute x-ray and neutron yields, Phys. Rev. E **106**, L013201 (2022).

[7] S. P. Regan *et al.*, Dependence of hot-spot mix in DT cryogenic implosions on the design adiabat, Bull. Am. Phys. Soc. **63**, BAPS.2018.DPP.UO4.10 (2018).

[8] R. C. Shah, S. X. Hu, I. V. Igumenshchev, J. Baltazar, D. Cao, C. J. Forrest, V. N. Goncharov, V. Gopalaswamy, D. Patel, F. Philippe, W. Theobald, and S. P. Regan, Observations of anomalous x-ray emission at early stages of hot-spot formation in deuterium-tritium cryogenic implosions, Phys. Rev. E **103**, 023201 (2021).

[9] D. Haberberger, A. Shvydky, V. N. Goncharov, D. Cao, J. Carroll-Nellenback, S. X. Hu, S. T. Ivancic, V. V. Karaseiv, J. P. Knauer, A. V. Maximov, and D. H. Froula, Plasma density measurements of the inner shell release, Phys. Rev. Lett. **123**, 235001 (2019).

[10] S. Zhang and S. X. Hu, Species separation and hydrogen streaming upon shock release from polystyrene under inertial confinement fusion conditions, Phys. Rev. Lett. **125**, 105001 (2020).

[11] D. Patel *et al.*, Effects of laser bandwidth in direct-drive high-performance dt-layered implosions on the omega laser, Phys. Rev. Lett. **131**, 105101 (2023).

[12] I. V. Igumenshchev *et al.*, Three-dimensional hydrodynamic modeling of omega direct-drive cryogenic implosions with highest fusion yield, Bull. Am. Phys. Soc. **64**, BAPS.2019.DPP.NO5.6 (2019).

[13] V. N. Goncharov, D. Cao, and R. C. Shah, The role of secular growth caused by mass modulations in inertial confinement fusion implosions, Bull. Am. Phys. Soc. **65**, BAPS.2023.DPP.UO07.10 (2023).

[14] T. C. Sangster *et al.*, Improving cryogenic deuterium–tritium implosion performance on omega, Phys. Plasmas **20**, 056317 (2013).

[15] J. Delettrez, R. Epstein, M. C. Richardson, P. A. Jaanimagi, and B. L. Henke, Effect of laser illumination nonuniformity on the analysis of time-resolved x-ray measurements in uv spherical transport experiments, Phys. Rev. A **36**, 3926 (1987).

[16] A. Lees *et al.*, Experimentally inferred fusion yield dependencies of omega inertial confinement fusion implosions, Phys. Rev. Lett. **127**, 105001 (2021).

[17] F. J. Marshall and J. A. Oertel, A framed monochromatic x-ray microscope for ICF (invited), Rev. Sci. Instrum. **68**, 735 (1997).

[18] D. Cao, R. C. Shah, S. P. Regan, R. Epstein, I. V. Igumenshchev, V. Gopalaswamy, A. R. Christopherson,

W. Theobald, P. B. Radha, and V. N. Goncharov, Interpreting the electron temperature inferred from x-ray continuum emission for direct-drive inertial confinement fusion implosions on omega, Phys. Plasmas **26,** 082709 (2019).

[19] I. V. Igumenshchev, A. L. Velikovich, V. N. Goncharov, R. Betti, E. M. Campbell, J. P. Knauer, S. P. Regan, A. J. Schmitt, R. C. Shah, and A. Shvydky, Rarefaction flows and mitigation of imprint in direct-drive implosions, Phys. Rev. Lett. **123,** 065001 (2019).

[20] I. V. Igumenshchev *et al.*, Three-dimensional hydrodynamic hydrodynamic simulations of the effects of laser imprint in omega implosions, Bull. Am. Phys. Soc. **62,** BAPS.2017 .DPP.CO8.11 (2017).

[21] S. X. Hu, V. N. Goncharov, P. B. Radha, J. A. Marozas, S. Skupsky, T. R. Boehly, T. C. Sangster, D. D. Meyerhofer, and R. L. McCrory, Two-dimensional simulations of the neutron yield in cryogenic deuterium-tritium implosions on OMEGA, Phys. Plasmas **17,** 102706 (2010).

[22] S. X. Hu, G. Fiksel, V. N. Goncharov, S. Skupsky, D. D. Meyerhofer, and V. A. Smalyuk, Mitigating laser imprint in direct-drive inertial confinement fusion implosions with high-z dopants, Phys. Rev. Lett. **108,** 195003 (2012).

[23] G. Fiksel, S. X. Hu, V. A. Goncharov, D. D. Meyerhofer, T. C. Sangster, V. A. Smalyuk, B. Yaakobi, M. J. Bonino, and R. Jungquist, Experimental reduction of laser imprinting and Rayleigh–Taylor growth in spherically compressed, medium-Z-doped plastic targets, Phys. Plasmas **19,** 062704 (2012).

[24] S. X. Hu, D. T. Michel, A. K. Davis, R. Betti, P. B. Radha, E. M. Campbell, D. H. Froula, and C. Stoeckl, Understanding the effects of laser imprint on plastic-target implosions on omega, Phys. Plasmas **23,** 102701 (2016).

[25] R. Betti, V. N. Goncharov, R. L. McCrory, and C. P. Verdon, Growth rates of the ablative Rayleigh–Taylor instability in inertial confinement fusion, Phys. Plasmas **5,** 1446 (1998).

[26] S. W. Haan, Onset of nonlinear saturation for Rayleigh-Taylor growth in the presence of a full spectrum of modes, Phys. Rev. A **39,** 5812 (1989).

[27] V. N. Goncharov *et al.*, Improving the hot-spot pressure and demonstrating ignition hydrodynamic equivalence in cryogenic deuterium–tritium implosions on omega, Phys. Plasmas **21,** 056315 (2014).

[28] D. Harding, M. Bonino, W. Sweet, M. Schoff, A. Greenwood, N. Satoh, M. Takagi, and A. Nikroo, Properties of vapor-deposited and solution-processed targets for laser-driven inertial confinement fusion experiments, Matter Radiat. Extremes **3,** 312 (2018).

[29] D. R. Harding and W. T. Shmayda, Stress- and radiation-induced swelling in plastic capsules, Fusion Sci. Technol. **63,** 125 (2013).